



CHORUS

This is the accepted manuscript made available via CHORUS. The article has been published as:

Nanosecond rf-Power Switch for Gyrotron-Driven Millimeter-Wave Accelerators

S.V. Kutsaev, B. Jacobson, A.Yu. Smirnov, T. Campese, V.A. Dolgashev, V. Goncharik, M. Harrison, A. Murokh, E. Nanni, J. Picard, M. Ruelas, and S.C. Schaub

Phys. Rev. Applied **11**, 034052 — Published 21 March 2019

DOI: [10.1103/PhysRevApplied.11.034052](https://doi.org/10.1103/PhysRevApplied.11.034052)

NANOSECOND RF POWER SWITCH FOR GYROTRON-DRIVEN MILLIMETER-WAVE ACCELERATORS

S.V. Kutsaev^{1,}, B. Jacobson^{2,#}, A.Yu. Smirnov¹, T. Campese¹, V.A. Dolgashev², V. Goncharik³,
M. Harrison¹, A. Murokh¹, E. Nanni², J. Picard⁴, M. Ruelas¹, S.C. Schaub⁴*

¹*RadiaBeam Technologies LLC, 1717 Stewart St, Santa Monica, CA 90403, USA*

²*SLAC National Accelerator Laboratory, 2575 Sand Hill Rd, Menlo Park, CA 94025, USA*

³*Logicware Inc, New York, NY 11235, USA*

⁴*Massachusetts Institute of Technology, 77 Massachusetts Ave, Cambridge, MA 02139, USA*

Abstract

The development of novel mm-wave high-gradient, > 200 MV/m, accelerating structures offers a promising path to reduce the cost and footprint of future TeV-scale linear colliders, as well as linacs for industrial, medical and security applications. The major factor limiting accelerating gradient is vacuum RF breakdown. The probability of such breakdowns increases with pulse length. For reliable operation, millimeter-wave structures require nanoseconds long pulses at the megawatt level. This power is available from gyrotrons, which have a minimum pulse length on the order of microseconds. To create shorter pulses and to reliably detect RF breakdowns we have developed the following devices: a laser-based RF switch capable of selecting 10 ns long pulses out of the microseconds long gyrotron pulses, thus enabling the use of the gyrotrons as power sources for mm-wave high gradient linacs, and a shot-to-shot sub-THz spectrometer with high-frequency resolution, capable of detecting pulse shortening due to RF breakdowns.

In this paper, we will describe the principle of operation of these devices and their achieved parameters. We will also report on the experimental demonstration of these devices with the high power gyrotron at the Massachusetts Institute of Technology. In the experiments, we demonstrated nanosecond RF power modulation, shot-to-shot measurements of the pulse spectra, and detection of RF breakdowns.

Keywords: nanosecond switch, shot-to-shot THz spectrometer, mm-wavelength structures, W-band, THz accelerators, high-gradient accelerating structure, vacuum RF breakdown;

1. Introduction

The development of novel high-gradient accelerating structures operating at THz frequencies is critical for future free-electron lasers [1] and TeV scale linear colliders [2]. These facilities will open new horizons in chemical [3] and biological imaging [4], and high energy physics [5]. The demand to reach high energies within a reasonable length requires high accelerating gradients beyond 100 MV/m [6].

* Corresponding author: kutsaev@radiabeam.com

Work performed while at RadiaBeam Technologies, Santa Monica, California 90404, USA

35 Recently there has been a significant effort at SLAC National Accelerator Laboratory to push the
36 operating frequency of linacs into W-band and beyond, with beam-driven 100 and 200 GHz
37 accelerating structures [7,8], and gyrotron-driven 100 and 300 GHz structures [9,10]. These metal
38 structures are made of two halves. The cavities are symmetrically milled into flat sides of metal
39 blocks. When the two halves are placed together, they form an accelerating structure.

40 To reach high gradients, such structures require MW-level RF power. Experiments with beam-
41 driven structures have shown that at these power levels the RF pulses should be shorter than a few
42 nanoseconds [11] for breakdown-free operation. Currently, the power sources capable of
43 producing the megawatt power levels in this frequency range are gyrotrons, which generate
44 microsecond-long pulses [12]. Therefore, gyrotron pulses have to be shortened in order to be fed
45 into accelerating structures. In this paper, we describe a laser-based RF switch capable of selecting
46 a several-nanosecond-long portion of a few-microsecond-long 1.5 MW 110 GHz pulse.

47 RF breakdowns limit the working power and produce irreversible surface damage in high power
48 RF components, including accelerating cavities and sources [13]. They cause pulse shortening of
49 the transmitted RF pulse, which results in a broadening of its spectrum. This spectrum broadening
50 can be detected with a frequency spectrometer. Therefore, to commission the RF switch and
51 reliably detect breakdowns in accelerating structures, we developed a shot-to-shot sub-THz
52 spectrometer with high-frequency resolution.

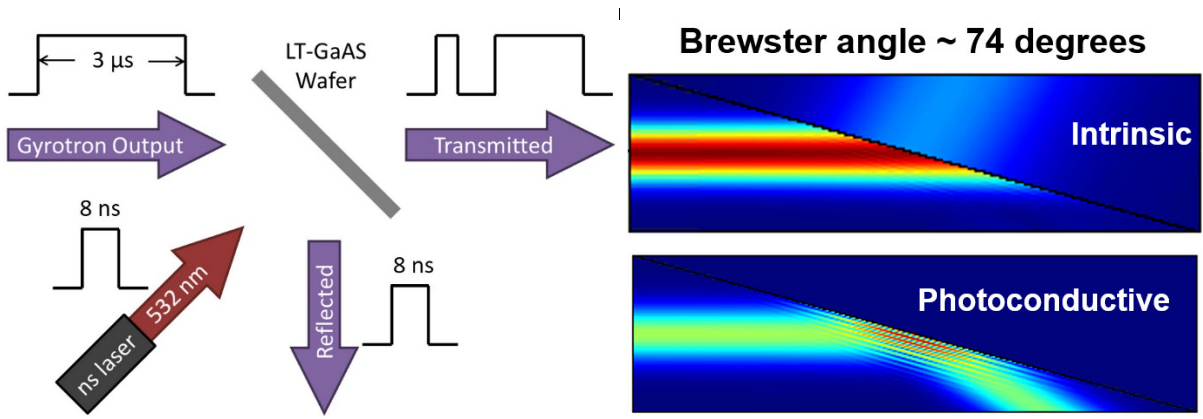
53

54 **2. RF switch design**

55 In order to selectively shorten the long pulse generated by the gyrotron, it is possible to implement
56 light-controlled semiconductor shutters [14,15] via the photoconductive effect. While it is known
57 that typical dielectric materials are transparent to microwaves, RF radiation reflects from metallic
58 interfaces. In the case of semiconductors, which behave similarly to metals through the generation
59 of free carriers from irradiation by light with photon energies above the material's band gap [16],
60 both transparent and reflective states can be realized. Therefore, if illuminated by a short laser
61 pulse, the two states of the semiconductor operate as a photo-gated switch for microwaves.

62 This principle of operation is depicted in Figure 1, left. A long microwave pulse is incident on a
63 semiconductor wafer. Illumination by a short laser pulse stimulates the photoconductive state of
64 the wafer, picking out and reflecting a short RF pulse as output for device testing. After the laser
65 pulse is off, the wafer returns to the intrinsic state and transmits the remainder of the microwave
66 pulse.

67



68

69

70

71

Figure 1: Simplified geometry (left) and Brewster angle incidence (right) configurations of gated window. COMSOL multiphysics simulation results show the transmission (top right) of 100 GHz through the intrinsic semiconductor and reflection (bottom right) from the interface in the photoconductive state.

72

COMSOL simulations of a 100 GHz wave interacting with the photoconductive state of the wafer

73

exhibiting high reflectivity are shown in the bottom right of Figure 1. In this model, the low

74

conductivity of the GaAs intrinsic state was assigned a conductivity of 1360 S/m which

75

corresponds to a photoinduced carrier concentration of $N = 10^{22} \text{ m}^{-3}$.

76

The refractive index ($n \approx 3.6$ for GaAs) of the semiconductor in the intrinsic state causes some

77

unwanted reflection of the incoming THz wave. To eliminate any power in the reflected beam

78

when the laser is off that could be delivered to the structure under test, we exploit Brewster angle

79

incidence [17]. For a polarized source incident at the Brewster angle, the reflected power is zero

80

in the intrinsic state, as shown in the top right panel of Figure 1. In testing the Brewster angle for

81

each wafer is altered to account for the different index of the particular material.

82

Surface plasma model of free charge carriers

83

Free charge carriers in materials distribute due to electrostatic forces, finding equilibrium arranged

84

in a thin plasma-like layer at the material surface. The interaction of this surface plasma with an

85

EM wave can be modeled as a media of a frequency dependent complex index of refraction. A

86

plasma frequency ω_p related to the charge carrier density, N , can be defined as: $\omega_p^2 = \frac{Ne^2}{\epsilon_0 m^*}$ where

87

e is the universal charge quanta, ϵ_0 the permittivity of free space, and m^* the effective mass of the

88

charge. In such a plasma, the frequency dependence of the relative dielectric function is given by:

89

$\epsilon(\omega) = 1 - \frac{\omega_p^2}{\omega^2}$. When $\omega < \omega_p$, ϵ becomes negative and the index of refraction becomes complex,

90

and only higher frequencies propagate through the plasma.

91

In the semiconductor intrinsic state, GaAs has a carrier density of $N_{intr} \sim 10^{12} \text{ m}^{-3}$. The plasma

92

frequency in this state corresponds to $\sim 35 \text{ MHz}$; 100 GHz waves freely propagate through the

93

surface. Stimulating the photoconductive state increases the carrier concentration by orders of

94

magnitude. At a carrier concentrations of $N_{phot} \sim 10^{19} \text{ m}^{-3}$ the plasma frequency is 100 GHz. At

95

higher carrier densities the wafer will begin to reflect the gyrotron power.

96

Photon absorption and carrier generation

97

A simple model of photon absorption and carrier production in the semiconductor is used: every photon absorbed generates one electron-hole pair and the charge generation rate, g , is the same as

98

the photon absorption rate. The absorption of light leads to attenuation following Beer's law:

99

100

$I(x) = I_0 \exp(-\alpha x)$ where I_0 is the optical power flux (in W/m^2) incident at the surface, x is the penetration depth into the wafer, and α is the frequency dependent linear absorption coefficient

101

102

[18]. The exponential decay of Beer's law implies that the majority of the optical power is absorbed in a layer of material $d = 1/\alpha$ thick. For example, at 532 nm the absorption coefficient in GaAs

103

104

is $\alpha = 7.9 \times 10^4 \text{ cm}^{-1}$ and the photons are absorbed in a thin layer $d \sim 0.1 \mu\text{m}$. However at 110 GHz, far below the conduction band gap energy, the absorption coefficient is $\alpha \sim 0.4 \text{ cm}^{-1}$

105

106

and $d \sim 2.5 \text{ cm}$. At this frequency there is almost no attenuation through a sub-mm-thick wafer.

107

In order to estimate the charge carrier density generated, consider illumination by uniform plane wave with a power flux I_0 [W/m^2] and the photon absorption within a layer $d = 1/\alpha$. To calculate

108

109

the photon density within this layer, the power flux is averaged as it is attenuated from the surface to the bottom of the layer. The average intensity is $I_{ave} = 0.63 I_0$. For this estimation we assume

110

111

that the photon absorption is uniformly distributed throughout the volume of the thin surface layer and generates a uniform charge density equal to the number of photons in this volume.

112

113

The charge carrier density generation rate g , measured in SI units of $\text{s}^{-1}\text{m}^{-3}$, is then $g = I_{ave}/(E_\gamma d)$, where E_γ is the energy of the absorbed photon. During illumination, an

114

115

equilibrium between charge carrier generation and recombination is reached. The increase in charge density during this photoconductive steady state is $\delta N = g\tau$, where τ is the recombination

116

117

time, or in terms of illumination and material parameters:

118

$$\delta N = \frac{0.63 I_0 \alpha \tau}{E_\gamma} \quad (1)$$

119

However once the illuminating pulse turns off, charge generation ceases, and carriers are removed from the conduction band through recombination. The time scale for the charge density, N , to

120

121

exponentially decay and return to the intrinsic state, thus turning off the laser-induced microwave reflectivity, is the recombination time τ . GaAs has a fast ($\tau_{GaAs} \sim 10 \text{ ns}$) recombination time,

122

123

which is comparable to the required pulse lengths [19] and is a good match for this application.

124

We also tested an undoped Si wafer which has a recombination time of $\tau_{Si} \sim 1 \mu\text{s}$, producing a reflectivity that decays 100 times more slowly, as shown in our measurements in Figure 10.

125

126

Drude-Lorentz model of complex dielectric function in photoconductive state

127

The simple plasma model of the dielectric function's frequency dependence provides an intuitive insight of the behavior of semiconductors in the photoconductive state, however it does not account

128

129

for interactions amongst the conduction band charge carriers. The Lorentz oscillator equation is a

130 more general model which includes the physical interactions between bulk electrons (polarization)
 131 and the incident electric field (through the ω_p term), damping caused by charge carrier collisions
 132 (the Γ term), and a line resonance (the ω_0 term). Here ϵ_∞ is a real constant representing the high-
 133 frequency asymptotic limit and the dielectric function is complex, $\epsilon = \epsilon' + i\epsilon''$.

$$134 \quad \epsilon(\omega) = \epsilon_\infty + \frac{\omega_p^2}{\omega_0^2 - \omega^2 + i\omega\Gamma}$$

135 This relation can be further simplified in the case of metals and can be analyzed using a modified
 136 form, the Drude-Lorentz model of permittivity [20], where the line resonance is set to DC since
 137 electrons in the conduction band do not experience the restoring force felt by electrons in bound
 138 states. This is also true for photogenerated electron-hole pairs excited to the conduction band in
 139 semiconductors. The damping coefficient corresponds to the carrier collision time, $\Gamma = 2\pi/\tau_{col}$,
 140 which is related to the carrier mobility μ and effective mass m^* by $\tau_{col} = \frac{\mu m^*}{e}$. The collision time
 141 is much shorter than the recombination time, in GaAs $\tau_{col} \sim 0.3 \text{ ps}$ and in Si $\tau_{col} \sim 0.1 \text{ ps}$, and is
 142 different from the *recombination time*, τ , relating the charge generation rate to the induced carrier
 143 density, $\delta N = g\tau$, in the photoconductive steady state. With these substitutions, the real and
 144 imaginary dielectric functions are given by:

$$145 \quad \epsilon'(N, \omega) = \epsilon_\infty - \frac{\frac{Ne^2 m^*}{\epsilon_0}}{(m^* \omega)^2 + \left(\frac{2\pi e}{\mu}\right)^2} \quad (2)$$

146 and

$$147 \quad \epsilon''(N, \omega) = \frac{\frac{2\pi Ne^3}{\mu \epsilon_0}}{(m^*)^2 \omega^3 + \omega \left(\frac{2\pi e}{\mu}\right)^2} \quad (3)$$

148 **Estimation of switch illumination power requirements**

149 The complex refractive index, $\tilde{n} = n + ik$, can be computed as a function of carrier concentration
 150 and frequency using the Drude-Lorentz model dielectric function, and the physical properties
 151 (effective mass and mobility) of a particular semiconductor material. The real (n) and imaginary
 152 (k) components of the complex refractive index are related to the dielectric function $\epsilon(N, \omega)$ by:

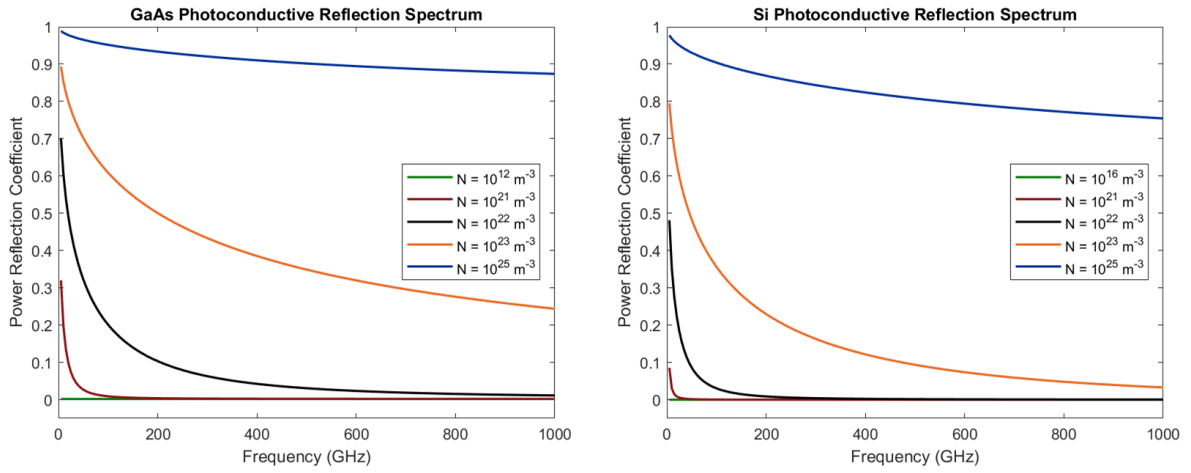
$$153 \quad n(N, \omega) = \sqrt{(|\epsilon| + \epsilon')/2} \text{ and } k(N, \omega) = \sqrt{(|\epsilon| - \epsilon')/2}.$$

154 The fraction of microwave reflected power can be computed from the complex refractive index by
 155 writing the ansatz $n \rightarrow \tilde{n}(N, \omega)$ in the Fresnel equation for the electric field reflectivity coefficient.

156 The expression for the power reflection coefficient of p-polarized waves traveling in air (angle of
 157 incidence θ_i , and angle of transmission θ_t) from the semiconductor is:

$$R = r_p r_p^* = \frac{(n^2 + k^2) \cos^2 \theta_i - 2n \cos \theta_i \cos \theta_t + \cos^2 \theta_t}{(n^2 + k^2) \cos^2 \theta_i + 2n \cos \theta_i \cos \theta_t + \cos^2 \theta_t} \quad (4)$$

158
 159 The reflected power coefficients are plotted as a function of frequency up to 1 THz in Figure 2 for
 160 carrier concentrations that increase from the semiconductor intrinsic state (without illumination)
 161 to highly photoconductive charge densities. In all cases, the RF wave is incident at Brewster's
 162 angle, calculated from values widely accepted in the literature which are appropriate for 110 GHz.
 163 The geometry used in this analysis is fixed for each material: for GaAs, $\theta_i = 74.4^\circ$ and $\theta_t = 15.6^\circ$;
 164 for Si, $\theta_i = 73.7^\circ$ and $\theta_t = 16.3^\circ$. The plots show that at the highest charge density considered
 165 the power reflection coefficient exceeds 90% at 110 GHz for each material.

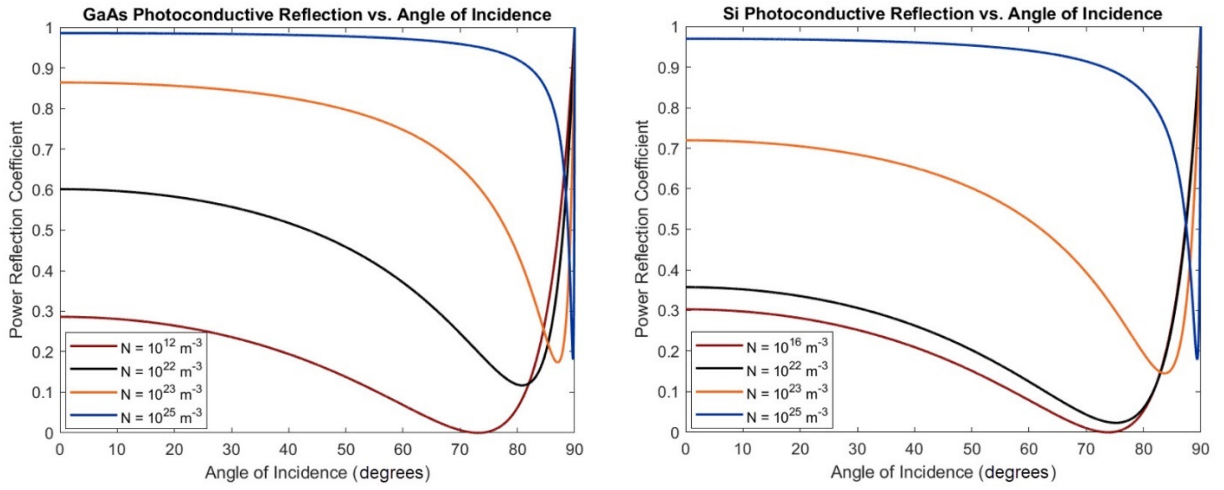


166
 167 *Figure 2: Power reflection coefficient for GaAs (left) and Si (right) as a function of frequency for various carrier concentrations*
 168 *from intrinsic state (10^{12} m^{-3} in GaAs and 10^{16} m^{-3} in Si) to a highly photoconductive state 10^{25} m^{-3} .*

169 The angular dependence of the reflectivity for increasing charge concentrations is also modeled.
 170 Using the same ansatz, $n \rightarrow \tilde{n}(N, \omega)$, a modified Snell's law recasts the reflected power
 171 coefficient as a function of θ_i :

$$R = r_p r_p^* = \frac{(n^2 + k^2) \cos^2 \theta_i - 2n \cos \theta_i \sqrt{1 - \frac{\sin^2 \theta_i}{n^2 + k^2}} + 1 - \frac{\sin^2 \theta_i}{n^2 + k^2}}{(n^2 + k^2) \cos^2 \theta_i + 2n \cos \theta_i \sqrt{1 - \frac{\sin^2 \theta_i}{n^2 + k^2}} + 1 - \frac{\sin^2 \theta_i}{n^2 + k^2}} \quad (5)$$

173 The power reflection coefficient for various charge densities and evaluated at 110 GHz is plotted
 174 in Figure 3 as a function of θ_i . As the charge carrier concentration rises, the minimum in the power
 175 reflection coefficient curve shifts higher, toward glancing incidence, and becomes non-zero,
 176 eliminating the Brewster's effect. There are differences between the performance of the two
 177 materials at intermediate values of N , GaAs being more responsive to increased concentrations. In
 178 the highly photoconductive state, for $N = 10^{25} \text{ m}^{-3}$ in either material, the reflectivity profile
 179 becomes flat for all but very steep angles and $R \geq 0.9$ for incidence at Brewster's angle.



180

181

182

Figure 3: Power reflection coefficient evaluated at 110 GHz for GaAs (left) and Si (right) as functions of incidence angle for various carrier concentrations from intrinsic state (10^{12} m^{-3} in GaAs and 10^{16} m^{-3} in Si) to a highly photoconductive state 10^{25} m^{-3} .

183

184

185

186

Lastly, we consider the case again with the RF incident upon the wafer fixed in the Brewster's angle configuration and now for the frequency of interest in this application, $f = 110 \text{ GHz}$. The power reflection coefficients for GaAs and Si are plotted in the left panel of Figure 4 using Equation 4

187

$$R = r_p r_p^* = \frac{(n^2 + k^2) \cos^2 \theta_i - 2n \cos \theta_i \cos \theta_t + \cos^2 \theta_t}{(n^2 + k^2) \cos^2 \theta_i + 2n \cos \theta_i \cos \theta_t + \cos^2 \theta_t} \quad (4)$$

188

189

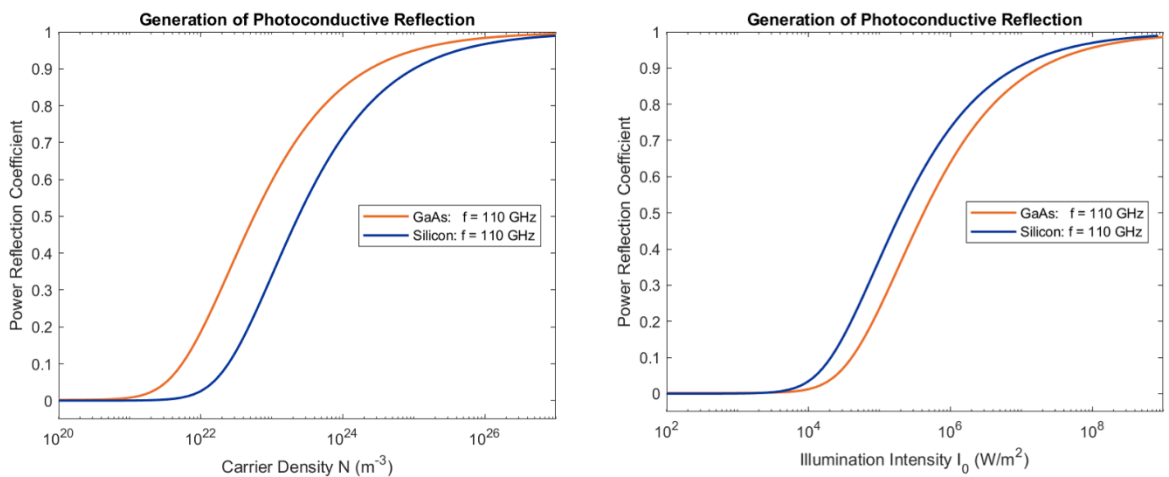
190

191

192

193

for fixed frequency and angles as a function of the carrier concentration density. Again the plot shows reflection coefficients exceeding 90% at $N = 10^{25} \text{ m}^{-1}$ in each material. This analysis also agrees with the previous two cases examining frequency and angular dependencies – in that for a given charge concentration, the GaAs material outperforms Si given that the photoinduced reflectivity is greater for the same charge concentration. Examination of Figure 4 (left) shows a horizontal shift between the two curves by roughly a factor of ~ 4 .



194

195

196

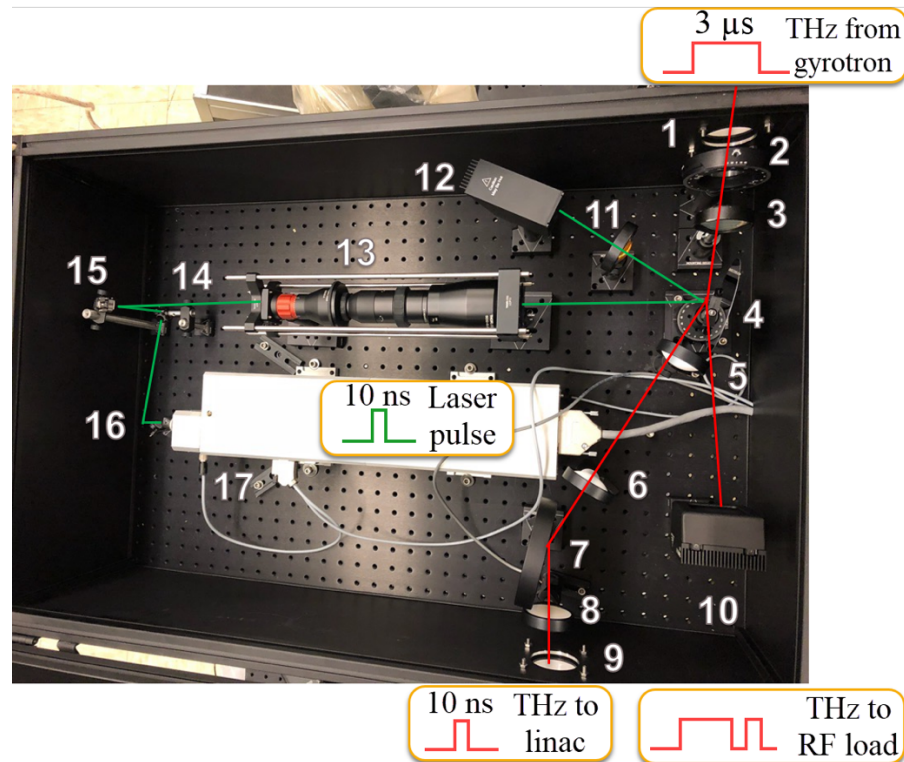
Figure 4: Power reflection coefficient evaluated at 110 GHz for GaAs and Si as functions of carrier concentration (left) and laser illumination intensity (right) in the Brewster's angle configuration. Note the apparent switch in responsivity from left to right.

197

198

The photoinduced charge density is converted by Equation 1 to a corresponding illumination intensity and is plotted in the right panel of Figure 4. It's notable that when plotted versus intensity,

199 the Si wafer outperforms GaAs by a factor of ~ 2.5 . Taking the ratio of Equation 1 for GaAs to Si
 200 reveals that almost 9 times the intensity is required for GaAs to generate the same charge density
 201 generated in Si. This explains the responsivity change: $9 \div 4 = 2.25 \cong 2.5$, which is the intensity
 202 Si light-to-charge generating over performance divided by the Si charge-to-reflectivity
 203 underperformance. In terms of intensity, the 90% threshold for the power reflection coefficient
 204 occurs when the wafer is illuminated by green 532 nm laser light of intensity 8 MW/m^2 for Si and
 205 by 20 MW/m^2 for GaAs.



206
 207
 208
 209
 210

Figure 5: Schematics of the laser-driven RF switch. 1- Input THz window, 2- Polarizer, 3 - THz lens #1, 4 – Wafer, 5 - THz lens #2, 6 - THz lens #3, 7 - Mirror, 8 - THz lens #4, 9 – Output THz window, 10 - THz load, 11 - Optical lens, 12 - Laser dump, 13 - Beam expander, 14 - Alignment mirror #1, 15 - Alignment mirror #2, 16 - Alignment mirror #3, 17 – 532 nm laser. Laser light is shown with green lines, THz signal with red lines.

211 Laser-driven RF switch prototype for high power bench test and evaluation

212 We have designed and constructed an enclosed tabletop version of the RF switching apparatus for
 213 the high-power experiment as shown in Figure 5. The 110-GHz radiation enters from the input
 214 window at the top, propagating down through the polarizer and Teflon THz lens. At the wafer, the
 215 THz pulse is switched; the long pulse enters the power dump and the short pulse is reflected by
 216 the wafer towards the gold mirror through the Teflon focusing lenses. This output pulse exits
 217 through the window for delivery to the device under test.

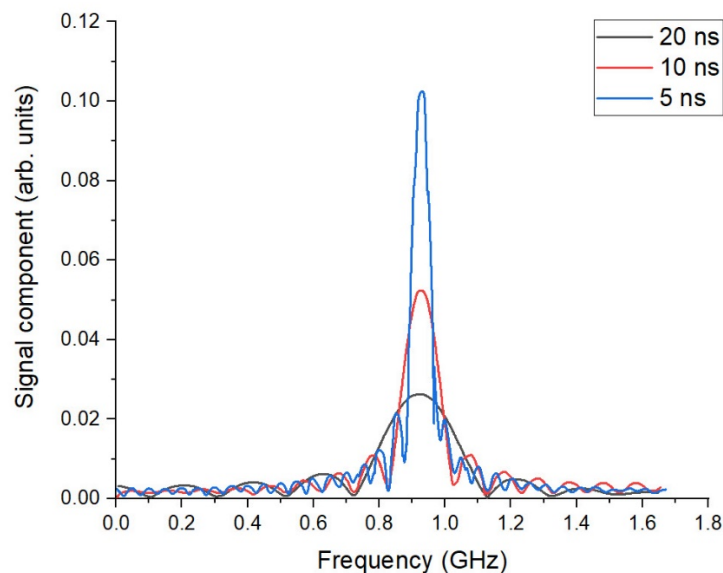
218 The wafer is illuminated by a Quantas Q1B-1064-10 electro-optically Q-switched diode-pumped
 219 Nd:YAG laser with second harmonic generation (SHG) unit. The SHG process produces 532 nm
 220 light in ~ 10 -ns pulses with a maximum repetition rate of 10 Hz. The maximum pulse energy of the
 221 green beam is 5 mJ and corresponds to a peak power of roughly 500 kW which, when (here

222 assumed to be uniform) illuminating a 4 cm diameter circle, produces an intensity of nearly
223 400 MW/m². The stimulated photo-carrier density for this illumination intensity is calculated to
224 be $N = 5 \times 10^{25} m^{-3}$ in GaAs, just above the maximum concentration plotted in Figure 2 and
225 Figure 3. For both GaAs and Si switches in this highly photoconductive state, the power reflection
226 coefficient exceeds about 90% at 110 GHz. Gallium arsenide performs slightly better than silicon
227 for a given switching illumination, as presented in Figure 4. Characterization of the system and
228 high power bench-test are described below.

229

230 3. Shot-to-shot spectrometer design

231 The idea of the super-heterodyne spectrometer is to mix the input signal with a central frequency
232 (f) and a signal from a local oscillator (LO) with a known frequency (f_0). The resulting signal will
233 have a component frequency of ($\Delta f = |f - f_0|$), which can be digitized and then analyzed with Fourier
234 Analysis. The actual input signal spectrum can be obtained by simply adding the LO frequency.
235 To solve the problem of the down-converted frequency ambiguity (below or above the LO
236 frequency), a quadrature mixer can be used, which will produce two signals, shifted by 90 degrees.
237 The sign of the relative phase will indicate the sign of Δf . The frequency resolution of this method
238 will be equal to $1/\Delta T$, where ΔT is the detected pulse length. Practically, for shorter pulses, we
239 will measure wider spectra due to this effect, as shown in Figure 6.



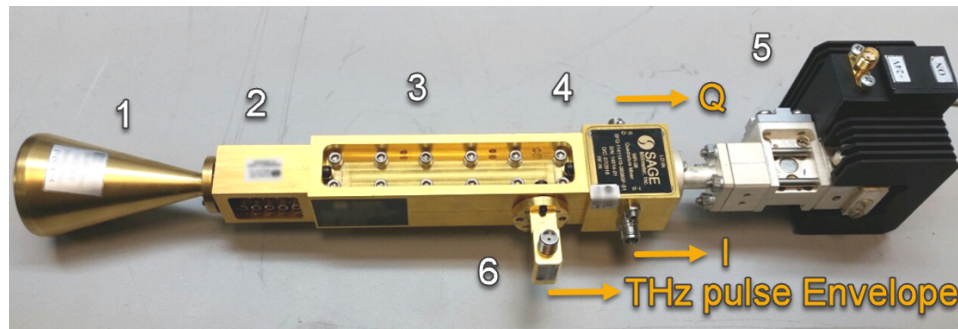
240

241

Figure 6. Calculated spectra of the single-frequency pulses with different pulse length.

242 In the designed spectrometer, the down-conversion heterodyne is formed with an input horn
243 antenna, 100-120 GHz band-pass WR-08 filter, 6 dB directional coupler, IQ-mixer and a local
244 oscillator with a fixed frequency of 110.08 GHz, corresponding to the MIT gyrotoron's frequency,
245 as shown in Figure 7. The design also incorporates a Schottky amplitude detector to observe the

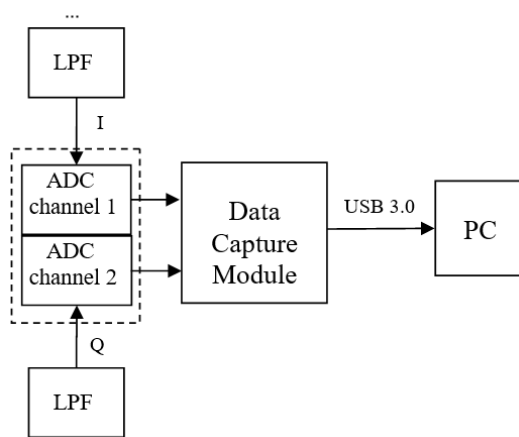
246 pulse shortening visually. The three signals (envelope, I and Q) are then digitized and Fourier-
247 analyzed.



248

249 *Figure 7. Detector part of the spectrometer. 1 – 30dB horn antenna, 2 – Band-pass filter, 3 – Directional coupler, 4 – IQ-mixer,*
250 *5 - Local oscillator, 6 – Schottky amplitude detector.*

251 Although the designed spectrometer can be connected to a fast oscilloscope for data acquisition,
252 the requirements for such a scope are very demanding, and the costs is high. Also, scopes cannot
253 provide shot-to-shot resolution for high repetition rates; for practical use, the pulse repetition rates
254 can be as high as 1 kHz. To solve this problem, we developed electronics for data acquisition and
255 processing.



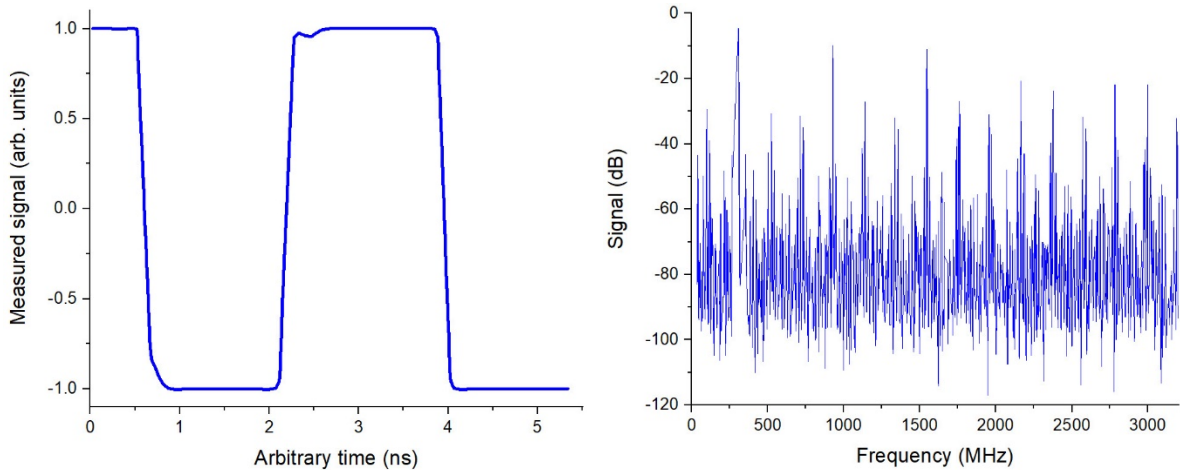
256

257 *Figure 8. The schematics (left) and the prototype (right) of the spectrometer data acquisition electronic board.*

258 The schematics of the developed data acquisition board is presented in Figure 8. The prototype
259 consists of the following modules: signal generator, analog-to-digital module, and a capture
260 module. The high-speed digital data from the capture module is transmitted to a PC. The analog-
261 to-digital module is a low-power, 12-bit RF-sampling analog-to-digital converter, operating in
262 single or dual channel regime at 6.4 or 3.2 GSPS, respectively. The converter has a buffered analog
263 input, integrated digital down converter with programmable numerically controlled oscillator and
264 decimation settings. The board has transformer-coupled analog inputs to accommodate a wide
265 range of signal sources and frequencies. The developed electronics boards are controlled through
266 an easy-to-use software program with a graphical user interface enabling quick configuration for
267 a variety of uses.

268 The current design has the following properties:

- 269 • Allows quick evaluation of ADC performance using TI HSDC Pro software;
- 270 • Direct connection to all TI modules using an FMC+ standard connector (backwards
- 271 compatible to FMC-equipped EVMs)
- 272 • JESD RX and TX IP cores with 16 routed transceiver channels and operating range from
- 273 1.6 Gbps to 15 Gbps
- 274 • Onboard high-speed USB 3.0-to-parallel converter bridges the FPGA interface to the host
- 275 PC and GUI
- 276 • 16-Gb DDR4 SDRAM (split into four independent 256×16 , 4-Gb SDRAMs; total of 1G
- 277 16-bit samples)



278
279 *Figure 9. Test synthesized 200 MHz signal digitization (left) and spectroscopy (right)*

280 The board was tested with the synthesized signal of 200 MHz including the digitization and Fourier
 281 analysis (see Figure 9). This test allowed us to demonstrate a proof-of-principle of the design and
 282 evaluate the requirements of the custom-made electronics that will be built for the future devices.
 283 In particular, we plan to build a custom-made board that will allow 3-channels, self-trigger regime
 284 and fast shot-to-shot data acquisition and spectrometry.

285

286 **4. Characterization and testing of the devices**

287 The mm-wave spectrometer and the RF switch have been tested to verify their proof-of-principle
 288 operations through high-power tests with a continuous wave (CW) 20 mW source and the MIT
 289 gyrotron. The experimental setup is shown in Figure 5. The optical source is a 532-nm, 8-ns pulse
 290 length, Q-switched laser. The laser beam is run through a beam-expanding array of lenses to
 291 prevent damage to the wafer and to illuminate more of the 100-mm-diameter. We used two wafers:
 292 silicon and GaAs. Measurements of the switched power from the CW 110 GHz source with both
 293 wafers are shown in Figure 10, demonstrating the orders of magnitude longer recombination time
 294 for silicon. The full-width-half-max (FWHM) of the GaAs reflecting mode is about 12-15 ns,
 295 while the FWHM of the silicon is about 6 μ s - 400 times longer. The rise time of both wafers is
 296 about 3 ns. Since pulse lengths of \sim 10 ns are required, the GaAs wafer is preferred for a single-
 297 wafer setup.

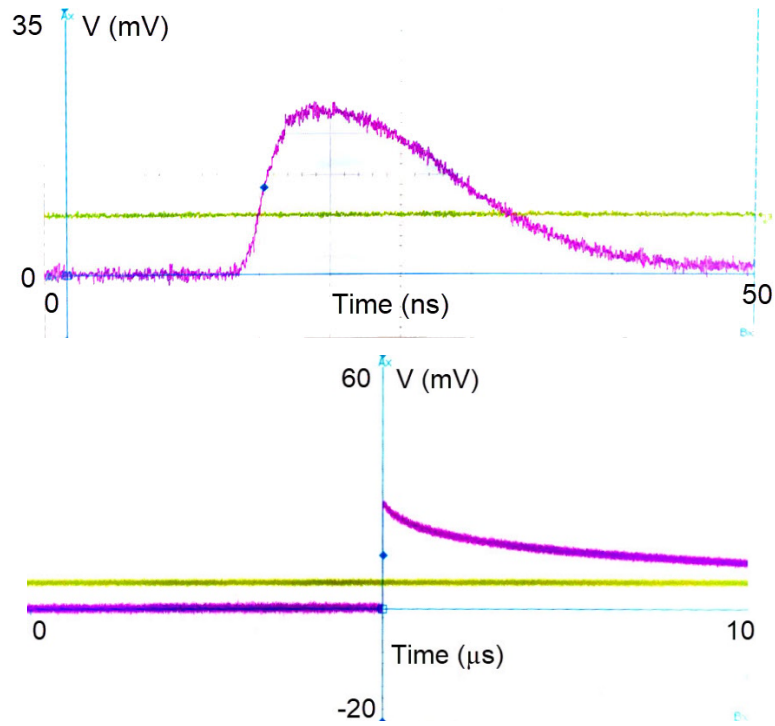


Figure 10: Oscillograms of the reflected THz signals after laser illumination of GaAs wafer (top) and a silicon wafer (bottom) measured with the Schottky amplitude detector. Note the different time scale on the plot demonstrating the significantly slower recombination time of Si relative to GaAs.

298 We have also used the 20 mW CW source at 110.08 GHz to characterize the power losses inside
 299 the switch. The microwave signal power was measured with the Schottky detector in different
 300 locations of the switch components in the layout. The results of these power measurements,
 301 presented in Table 1, suggest that in the current design, about half of the power is lost in the optical
 302 elements and 1/3 of the microwave power is lost on (transmitted through) the wafer and not
 303 reflected.

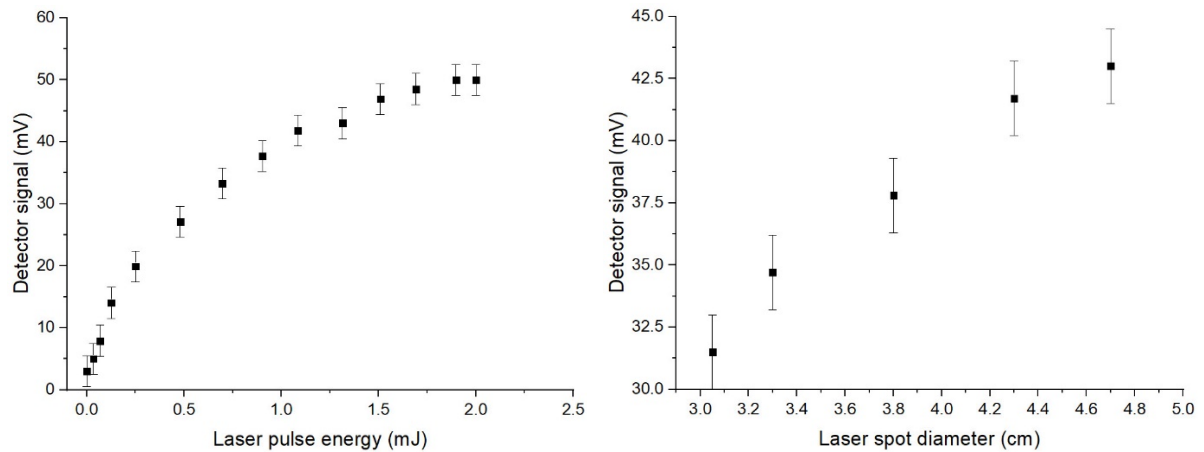
304 Table 1. Signal power measured in different locations of the switch component layout

Location	Schottky, mV	Power, %
Power source	220	100%
Input window	209	95%
Polarizer	182	82%
Lens 1	210	95%
Wafer (Cu)	135	61%
Output window (Si)	50	22%
Output window (Cu)	72	32%

305 We have then measured the power transmission of the switch as a function of laser beam
 306 parameters (laser pulse energy and beam spot size on the wafer) to understand the cause of power
 307 losses due to the wafers. The results of these measurements are shown in Figure 11 and suggest
 308 that although we have enough laser power (the signal nearly saturates), we could use a larger beam
 309 spot at the wafer. We have also imaged the laser beam spot profile on the wafer (Figure 12), which

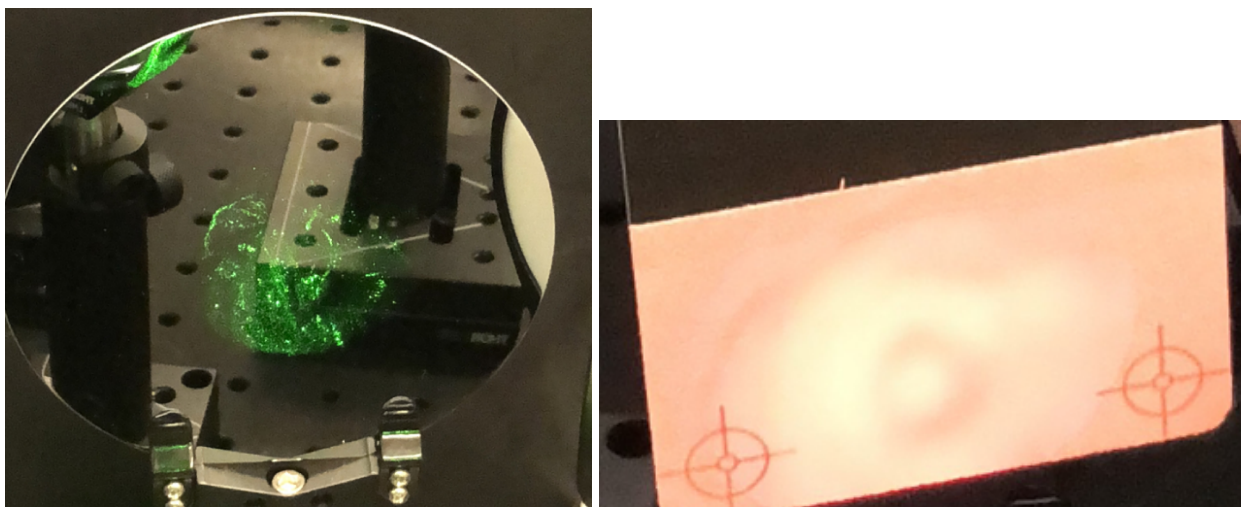
310 demonstrates some irregularities in laser intensity distribution that may also contributes to the
311 transmission reduction.

312 Although, the transmitted power is more than sufficient to achieve the required cavity gradients of
313 200 MV/m, in the future applications, the losses can be reduced by improving the laser beam
314 expander optics and replacing the lossy THz lenses by gold-plated off-axis parabolic mirrors. In
315 high repetition and high average power applications, it is especially important to induce very high
316 reflectivity to eliminate absorption and heating in the semiconductor switch.



317

318 *Figure 11. Transmitted signal measured by Schottky detector as a function of laser pulse energy using the maximum spot size of*
319 *4.7 cm (left) and as a function wafer spot diameter (right).*



320

321 *Figure 12. Laser beam spot profile measured at the wafer (left – as is, right - with a detector card).*

322 After the switch was tested and characterized with the low-power source, it was shipped to the
323 laboratory of Plasma Science and Fusion Center (PSFC) MIT to test its high-power performance
324 with the gyrotron. The gyrotron in its current configuration produces a 3 μ s pulse of 110 GHz
325 microwaves. The maximum output power is 1.1 MW. The gyrotron output coupler produces an
326 HE₁₁ mode in the output corrugated waveguide. This mode then couples with 98% efficiency into
327 a free space Gaussian beam with a 10.15 mm beam waist [21]. The nominal performance
328 parameters for the gyrotron are listed in Table 2 [12]. The gyrotron has two high power operating
329 points which can produce MW pulses. During this experimental stage, the operating parameters of

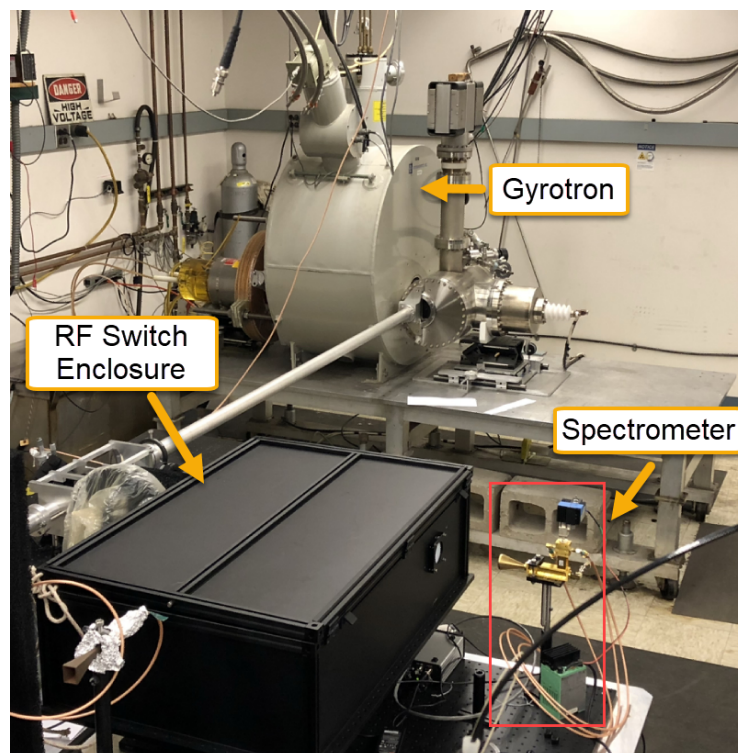
330 the gyrotron were set for the nominal 110.08 GHz frequency. The experimental setup of this test
331 is shown in Figure 13.

332

Table 2. MIT gyrotron nominal operating conditions

Nominal Frequency, GHz	110.08
Peak Power, MW	1.5
Pulse Length, μs	0.1-3
Bandwidth, GHz	+ 0.6
Rise Time, ns	100

333

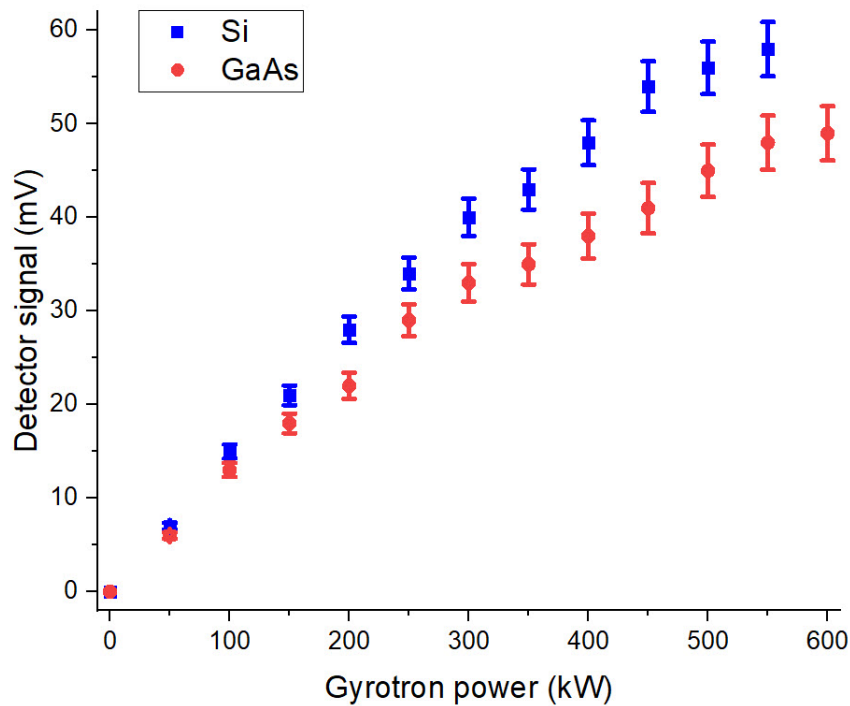


334

335

Figure 13. The experimental setup of the high-power tests of the laser-gated RF switch at MIT PSFC lab.

336 We gradually increased the microwave power from 0 to 600 kW. The gyrotron power limit of
337 600 kW was due to reflections from the device under test. We measured the switch output signal
338 with the Schottky detector and spectrometer. The test was performed with undoped Si and GaAs
339 wafers with identical laser and THz parameters and shown in Figure 14. Our measurement shows
340 that the reflectivity induced in the Si wafer is more sensitive to the laser power than the GaAs
341 wafer and qualitatively agree with the right plot of Figure 4. Stable operation with each wafer at
342 550 kW was reached. This power will produce an accelerating gradient above 200 MV/m in a
343 SLAC W-band accelerating structure [7], including the losses from the switch components.



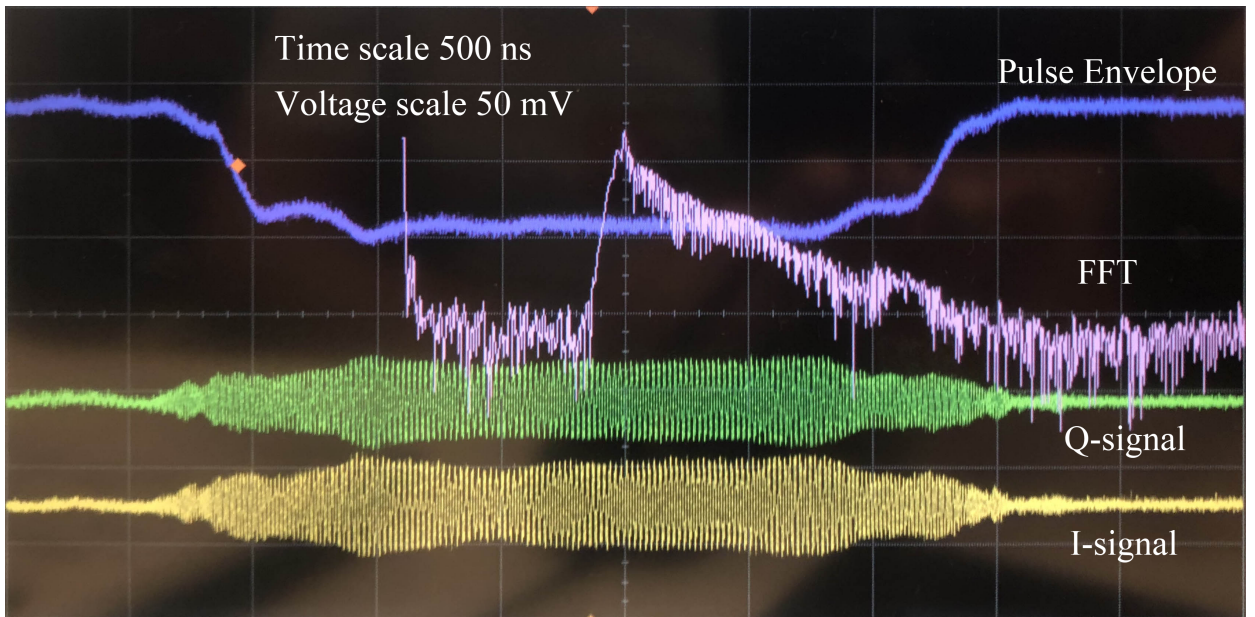
344

345 *Figure 14. Measured peak amplitude at the output of the switch as a function of gyrotron power. The vertical lines correspond to*
 346 *accelerating gradients of 100 and 200 MV/m in the SLAC mm-wave accelerating structure.*

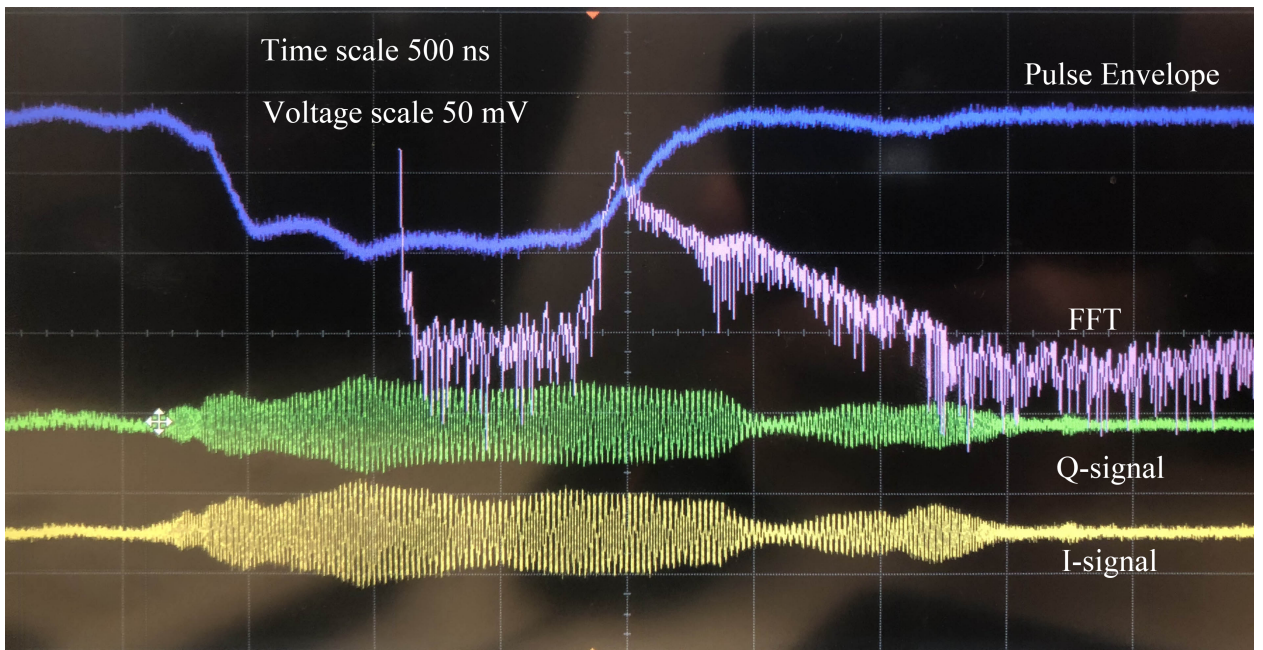
347 Finally, we checked the RF breakdown detection capabilities of our spectrometer. The breakdowns
 348 that were witnessed were not normal operation or inherent to the gyrotron. The gyrotron is output
 349 coupled to a 31mm corrugated waveguide. A mirror was required on the output of this waveguide
 350 in order to locate the RF switch enclosure within the space available in the lab.

351 When the RF reflects at a 90-degree angle, there's an enhancement of the electric field in certain
 352 regions up to a factor of 2 above the incident E-field intensity, similar to that, shown in Figure 1,
 353 right. The power is high enough from the gyrotron that, with that factor of 2, it reaches air-
 354 breakdown limit. When this happens, the microwaves are scattered/reflected back towards the
 355 gyrotron, which causes the output signal to be truncated. Each breakdown event was accompanied
 356 by the loud “bang” sound.

357 To register the breakdown, we put a copper disk in place of the semiconductor wafer in order to
 358 measure the full pulse length from the gyrotron. When breakdown occurs, the pulse length is
 359 shortened, while the frequency spectrum becomes wider as shown in Figure 15. We made shot-to-
 360 shot measurements over the 500 pulses at 1 Hz repetition rate. Pulse width, frequency bandwidth
 361 (FWHM), and shot-to-shot spectra were measured and are shown in Figure 16, which clearly
 362 demonstrates the capability of the spectrometer to detect RF breakdown events. The spikes are
 363 clearly seen in both pulse and spectrum width measurements.



364



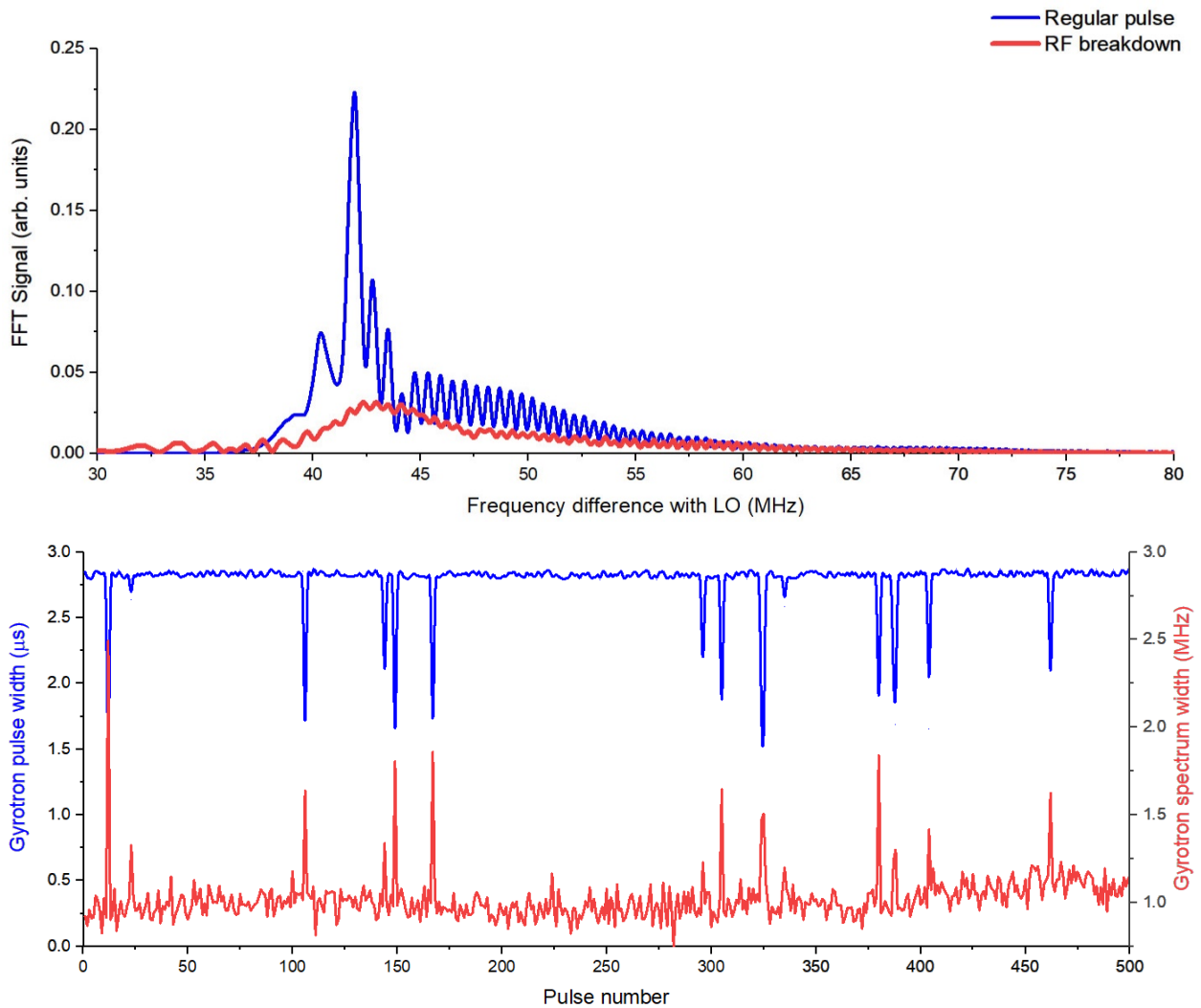
365

366

367

368

Figure 15. Scope traces of envelopes for non-breakdown (top) and breakdown (bottom) shots. The plot represents the following traces: blue - pulse envelope, yellow - I-signal, green - Q-signal, pink - FFT of I-signal. Time scale of the traces is 500 ns, and voltage scale is 50 mV for I- and Q- signals, and 10 mV for the envelope.



369

370

371 *Figure 16. Measured THz signal parameters. Top: single pulse spectra during regular (blue) and RF breakdown (red) events.*
 372 *Bottom: Pulse length (blue) and frequency spectrum FWHM width (red) of 500 consecutive RF pulses. Drops in pulse lengths and*
 373 *spikes in spectra represent breakdown events.*

374

Summary

375 Future accelerators for high energy particle physics and X-ray sources for biological and material
 376 research require miniaturized linacs. Development of compact mm-wave linacs will be
 377 advantageous in reducing the cost of future accelerator facilities. One issue in making such
 378 accelerators practical is the availability of a method to feed mm-wave RF power into these linacs.
 379 Currently, there are no mm-wave megawatt sources with nanosecond pulse lengths. Another issue
 380 is the absence of a method that reliably detects RF breakdowns, which damage the accelerating
 381 structures, and interrupts their operation.

382 To solve these issues, we developed a laser-based RF switch and a high-resolution shot-to-shot RF
 383 spectrometer. The switch allows selecting ~ 10 ns long pulses out of microseconds long pulses,
 384 thus enabling the use of the gyrotrons as the RF source for mm-wave high gradient linacs. The
 385 spectrometer is capable of reliably measuring nanosecond-long RF pulses, which is required to
 386 detect RF breakdowns.

387 We built and tested prototypes of both devices. The tests demonstrated the purity of the reflected
388 pulse without any reflection during the “off” state, RF power modulation up to 550 kW by the
389 switch, and shot-to-shot measurements of 110 GHz pulses by the spectrometer. We demonstrated
390 that our spectrometer reliably detects RF breakdowns. The switch and spectrometer will allow
391 advancement of compact mm-wave linacs, enabling miniaturization of many future accelerator
392 facilities. In addition to the applications for accelerators, these devices will find multiple
393 applications in the broader field of THz technology and diagnostics, as well as in W-band power
394 multipliers for military and telecommunication applications.

395

396 **Acknowledgments**

397 This work was supported by the U.S. Department of Energy, Office of High Energy Physics, under
398 SBIR grant DE-SC0013684. The work at MIT was supported by the Department of Energy, Office
399 of High Energy Physics, grant No. DE-SC0015566 and Office of Fusion Energy Sciences, grant
400 No. DE-FC02-93ER54186.

401

402 **References**

-
1. G.L. Carr, M.C. Martin, W.R. McKinney, K. Jordan, G.R. Neil and G.P. Williams, High-power terahertz radiation from relativistic electrons, *Nature* 420, 153-156 (2002).
 2. R. Temkin, M. Shapiro, US Workshop on High Gradient Research for Multi TeV Linear Colliders (2005).
 3. A.J. Huber, F. Keilmann, J. Wittborn, J. Aizpurua and R. Hillenbrand, Terahertz Near-Field Nanoscopy of Mobile Carriers in Single Semiconductor Nanodevices, *Nano Lett.* 8, 11 (2008).
 4. S. Wang, X-C. Zhang, Pulsed terahertz tomography, *J. Phys. D: Appl. Phys.* 37, 4 (2004).
 5. L. Linssen, A. Miyamoto, M. Stanitzki, and H. Weerts, Physics and Detectors at CLIC: CLIC Conceptual Design Report, *CERN Yellow Report* CERN-2012-003 (2012).
 6. M. Aicheler, P. Burrows, M. Draper, T. Garvey, P. Lebrun, K. Peach, N. Phinney, H. Schmickler, D. Schulte, N. Toge, A Multi-TeV Linear Collider Based on CLIC Technology: CLIC Conceptual Design Report, *CERN Yellow Report* CERN-2012-007 (2012).
 7. M. Dal Forno, V. Dolgashev, G. Bowde, C. Clarke, M. Hogan, D. McCormick, A. Novokhatski, B. Spataro, S. Weathersby and S.G. Tantawi, RF breakdown tests of mm-wave metallic accelerating structures, *Phys. Rev. Accel. Beams* 19, 011301 (2016).
 8. M. Dal Forno, V. Dolgashev, G. Bowden, C. Clarke, M. Hogan, D. McCormick, A. Novokhatski, B. O’Shea, B. Spataro, S. Weathersby, and S.G. Tantawi, RF breakdown measurements in electron beam driven 200 GHz copper and copper-silver accelerating structures, *Phys. Rev. Accel. Beams* 19, 111301 (2016).
 9. E. Nanni, V. Dolgashev, A. Haase, J. Neilson, S. Tantawi, S. Jawla, S.C. Schaub, R.J. Temkin and B. Spataro, Toward High-Power High-Gradient Testing of mm-Wave Standing-Wave Accelerating Structures, in *Proceedings of 9th International Particle Accelerator Conference*, Vancouver, Canada, 2018, p. 1224.
 10. E. Nanni, S. Schaub, M. Othman, V. Dolgashev, R. Li, M.C. Hoffmann, X. Wang, R. Temkin, B. Spataro, S. Tantawi, A. Haase, S. Jawla, J. Neilson, Jeffrey and J. Picard, High-Gradient Accelerators at THz Frequencies, in

Proceedings of 18th Advanced Accelerator Concepts Workshop, Breckenridge, CO, 2018 [in the process of being published].

11. M. Dal Forno, V. Dolgashev, G. Bowden, C. Clarke, M. Hogan, D. McCormick, A. Novokhatski, B. O'Shea, B. Spataro, S. Weathersby and S.G. Tantawi, High gradient tests of metallic mm-wave accelerating structures, *Nucl. Instrum. Methods Phys. Res A* 864, p.12-28 (2017).
12. E.M. Choi, C. Marchewka, I. Mastovsky, M.A. Shapiro, J.R. Sirigiri and R.J. Temkin, Megawatt Power Level 120 GHz Gyrotrons for ITER Start-Up, *J. Phys.: Conf. Ser.* 25, 1 (2005).
13. E.I. Simakov, V.A. Dolgashev, S.G. Tantawi, Advances in high gradient normal conducting accelerator structures, *Nucl. Instrum. Methods Phys. Res A* 907, p. 221-230 (2018).
14. S. Mitsudo, T. Furuya, Y. Shimoyama, T. Fujita, Y. Tatematsu, T. Idehara and T. Saito, Development of the millimeter wave pulsed ESR spectrometer, in *Proceedings of 34th International Conference on Infrared, Millimeter, and Terahertz Waves*, Busan, South Korea, 2009.
15. A. Rosen, P. Stabile, W. Janton, A. Gombar, J. Delmaster, P. Basile and R. Hurwitz, Optically Controlled Subsystems at HF and at mm-Wavelengths, *Microw. Opt. Technol. Lett.* 2, 11 (1989).
16. L.I. Glazman, Resonant excitation of carriers in a semiconductor by a high-power light pulse, *Sov. Phys. JETP* 53, 1 (1981).
17. D. Brewster, On the laws which regulate the polarization of light by reflection from transparent bodies, *Philosophical Transactions of the Royal Society of London* 105 (1815).
18. A. Beer, Bestimmung der Absorption des rothen Lichts in farbigen Flüssigkeiten, *Annalen der Physik und Chemie.* 86: 78–88 (1852) [in German].
19. M.E. Levinshtein, S.L. Rumyantsev, *Handbook Series on Semiconductor Parameters* (World Scientific, London, 1996), vol.1, pp. 77-103.
20. L. Rosenfeld, *Theory of Electrons* (Dover Publications, New York, 1965), p.68.
21. J.M. Neilson, R.L. Ives, S.C. Schaub, W.C. Guss, G. Rosenzweig, R.J. Temkin and P. Borchard, Design and High-Power Test of an Internal Coupler to HE₁₁ Mode in Corrugated Waveguide for High-Power Gyrotrons, *IEEE Trans. Electron Devices* 65, 6 (2018).